



Synthesis of $\text{La}_2\text{MnFe}_2\text{O}_7$ and $\text{La}_2\text{CuFe}_2\text{O}_7$ magnetic nanocomposites (nano mixed metal oxides) as efficient photocatalyst for organic dye removal

Somaye Khammarnia^{1,*}, Jilla Saffari², Mehri-Saddat Ekrami-Kakhki³

¹Chemistry Department, Payame Noor University, Tehran 19395-4697, Iran

²Department of Chemistry, Zahedan Branch, Islamic Azad University, P.O. Box 98135-978, Zahedan, Iran

³Esfarayen University of Technology, Esfarayen, North Khorasan, Iran

ARTICLE INFO

ABSTRACT

Article history:

Received 12 January 2024

Received in revised form 5 February 2024

Accepted 5 February 2024

Available 5 February 2024

Keywords:

Photocatalysts

Malachite green oxalate

Methyl violet

Eriochrome black T

Co-precipitation

In this work, $\text{La}_2\text{MnFe}_2\text{O}_7$ and $\text{La}_2\text{CuFe}_2\text{O}_7$ photocatalysts were synthesized using a co-precipitation method. The surface morphology, structure, crystalline phase and magnetic behavior of the catalysts were investigated by TEM, FT-IR, XRD, DRS, and VSM. The photocatalytic activity of the $\text{La}_2\text{MnFe}_2\text{O}_7$ and $\text{La}_2\text{CuFe}_2\text{O}_7$ nanocomposites were appraised using the optical decomposition of malachite green oxalate (MG), methyl violet (MV), and Eriochrome Black T (EBT) beneath ultraviolet (UV) beam irradiance at different factors like the solution pH, dyes' concentration, catalysts' amount, temperature and time of UV light radiation. This research presented the synthesis of new composite magnetic photocatalysts and their application in the photodegradation of dye pollutants.

1. Introduction

Nanotechnology introduces new solutions towards the growth of present technologies and in these solutions, issues such as health, environmental, and economic problems are touched [1-3]. There are environmental concerns all over the world. One of the most important issues in life is water treatment. There are various pollutants in water, among which organic contaminants have serious dangers [4-6]. Adjustable size and new mechanisms are the characteristics of nanoparticles, and these properties indicate promising technology. Therefore, under ultraviolet radiation, they are used as photocatalysts to eliminate the organic contaminants such as dyes [7, 8]. Nanocomposites have at least one component in nanometer dimensions [9]. Nanocomposites are appropriate alternatives to reduce the limitations of microcomposites, whereas posing procurement for controlling the primary combination

and stoichiometry within the nano cluster phase. They are posed to the preparation challenges due to their unique design and possession compositions that are not found in conventional materials. Nanocomposites have been introduced as materials from the twenty-first century. Although the first inference to them was reported in the beginning of 1992 [10], a popular conception of their properties has not still been obtained [11]. Organic dyes are colored and durable compounds and are extensively utilized in industrial manufacture of dyeing agents, textile, leather, paint, clothing, rubber, biological imaging, plastic paper making and food processes etc due to the utilizing a large volume of organic dyes are causing damage to human lungs, kidneys, organs and carcinogenic effects. The most common organic dyes are EBT, MO, MG, Congo red (CR), MB, and so on [12]. Many paper and waste industries as well as textile mills have discharged waste-polluted water containing hazardous contaminants into water bodies, which has resulted in serious

* Corresponding author.; e-mail: somayekhammarnia@pnu.ac.ir

<https://doi.org/10.22034/crl.2024.434922.1277>



This work is licensed under Creative Commons license CC-BY 4.0

contamination of water [13]. The entry of these industries' wastewater to the environment affects living organisms in aquatic ecosystems and human health [14]. As a result, purification of dye-polluted wastewaters via decontamination process is essential before their evacuation. The depletion of large values of dyes into wastewater is a serious threat for environmental sustainability and human health [15]. As a result, in aquatic ecosystems, the process of photosynthesis is affected. Also, due to the association of organic dyes in water with jaundice, cancer, skin stimulation, sensitivity, heart defects, and mutation, they have dangerous and toxic effects on human health [16]. Thus, to eliminate these organic dyes and to expand robust, economic, and environmentally sociable procedures, it is necessary to use a variety of techniques such as physicochemical [17, 18], chemical [19], biological [20], electrochemical [14] and advanced oxidation process-based approaches such as photo-Fenton's oxidation and Fenton's reagent systems to remove dyes from water. The production of strong radical components causes rapid decomposition of dyes [21-23]. Researchers have done many studies in the direction of wastewater decolorization [5, 24, 25]. In this field, metal oxides have been employed to decompose organic pollutants in water to reduce hazardous materials [26].

In this study, $\text{La}_2\text{MnFe}_2\text{O}_7$ and $\text{La}_2\text{CuFe}_2\text{O}_7$ magnetic nanocomposites were synthesized for the first time. These nanocomposites were synthesized using co-precipitation method and characterized through FTIR, TEM, DRS, XRD and VSM analyses. The photocatalytic activity of the synthesized nanocomposites was studied using MV, MG and EBT dyes as organic pollutant for the first time.

2. Experimental details

2.1. Methods and materials

$\text{Fe}(\text{NO}_3)_3 \cdot 9\text{H}_2\text{O}$, NaOH, $\text{LaCl}_3 \cdot 7\text{H}_2\text{O}$, $\text{CuCl}_2 \cdot 6\text{H}_2\text{O}$, $\text{MnCl}_2 \cdot 2\text{H}_2\text{O}$, $\text{Co}(\text{NO}_3)_2 \cdot 6\text{H}_2\text{O}$ as well as octanoic acid were purchased from Merck corporation. FT-IR spectra were recorded using Rayleigh (WQF-510A) FTIR spectrophotometer. A Philips X-ray diffractometer with Ni-filtered $\text{CuK}\alpha$ radiation was used for performing the X-ray diffraction measurements. The magnetic susceptibility measurements were performed via VSM (made by Meghnatis Daghigh Kavir Company, Kashan, Iran) at the applied sweeping magnetic field of $\pm 10,000$ Oe. Zeiss-EM10C-100 kV was used to take the TEM images. An ultrasonic irradiance was accomplished

using a multi-purpose ultrasonic generatrix (BandLine MS 73), equipped with a transformer and titanium oscillator, operated at 20 kHz with an almost 150 W power output. The registration of absorption spectra was done by a Perkin-Elmer LAMBDA45 UV/Vis spectrophotometer.

2.2. Synthesis of $\text{La}_2\text{MnFe}_2\text{O}_7$ and $\text{La}_2\text{CuFe}_2\text{O}_7$ nanocomposites

Three separate solutions were obtained by dissolving 0.01 mole of $\text{LaCl}_3 \cdot 7\text{H}_2\text{O}$, $\text{MnCl}_2 \cdot 2\text{H}_2\text{O}$ (or $\text{CuCl}_2 \cdot 6\text{H}_2\text{O}$) and $\text{Fe}(\text{NO}_3)_3 \cdot 9\text{H}_2\text{O}$ in 10 ml of distilled water. The prepared solutions in the previous step were mixed together, and 2 mL of octanoic acid added gradually as surfactant. Afterwards, the solution was stirred vigorously and NaOH 5 M solution added dropwise until the solution pH reached 8-9. After the complete precipitation, the solution was sonicated. The crystalline phase of nano-particles was obtained after 30 min/30 °C in 150 W and 20 kHz sonication. The white precipitate from sonication was purified and calcinated for 2 hours at 800 °C for removing the organic residue. The nanoparticles obtained by sonication has the highest purity.

2.3. Photocatalytic activity for degradation of dyes

To perform photocatalytic experiments, 10 mL of MV, MG and EBT aqueous solutions (0.001 M) were separately added to 20 mg of $\text{La}_2\text{MnFe}_2\text{O}_7$ and $\text{La}_2\text{CuFe}_2\text{O}_7$ nanocomposites. The suspension was magnetically stirred for 30 min in dark before irradiation. Afterward, the mixture was illuminated with UV light for one hour. These lamps were located around the outer level of the mixture. The effects of some factors such as temperature, solution pH, dyes' concentration, photocatalysts' amount as well as irradiation time were examined and optimized. At last, the reaction mixture was filtered, and the UV-Vis analysis performed to determine the residual concentration of MV, MG as well as EBT dyes. The residual adsorption of MV, MG and EBT by $\text{La}_2\text{MnFe}_2\text{O}_7$ nano-composite in several catalyst doses is shown in Fig. 1.

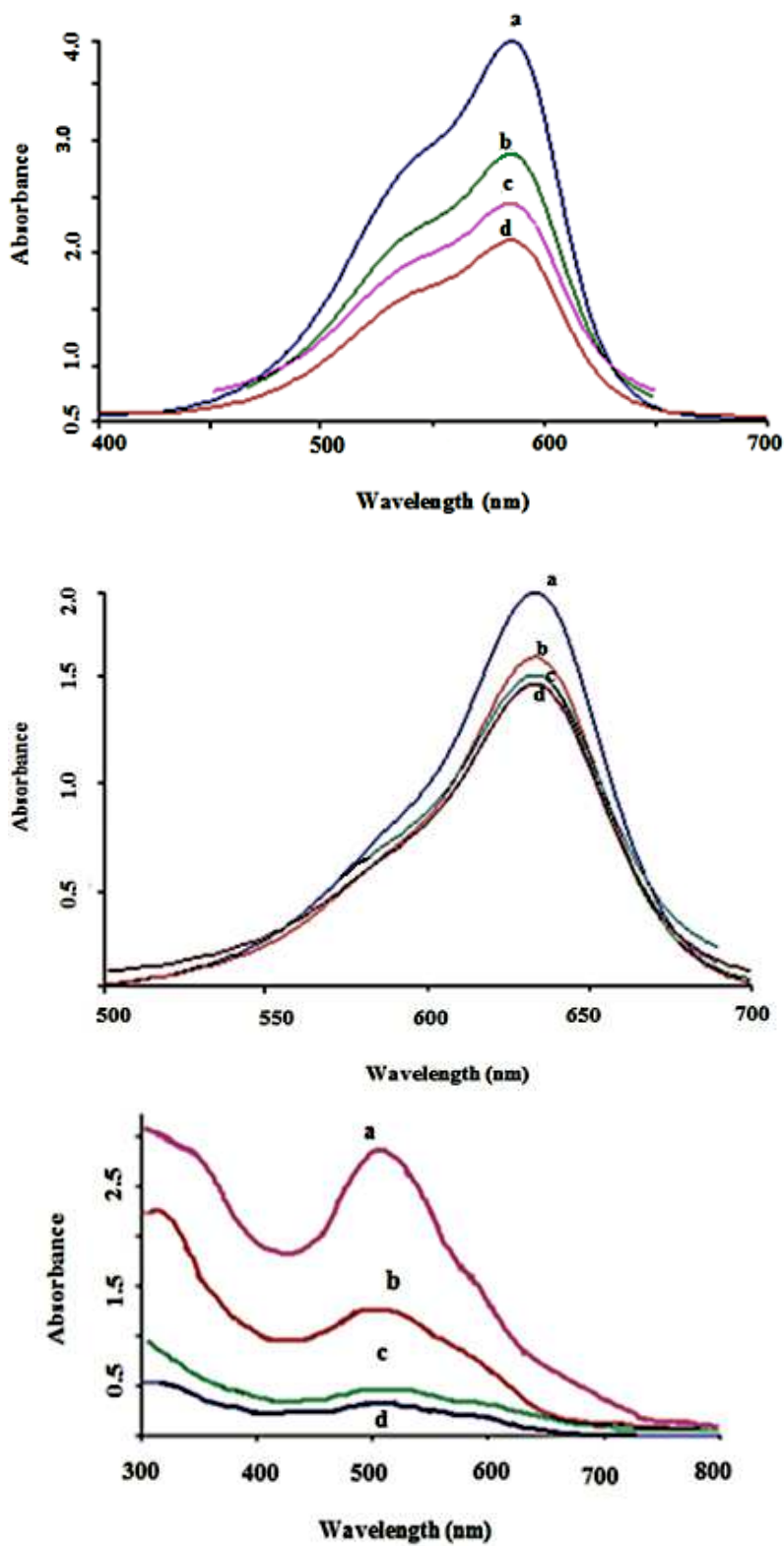


Fig. 1. UV-Vis absorption spectra of MV (up), MG (center) and EBT(down) with $\text{La}_2\text{CuFe}_2\text{O}_7$ nanoparticles after a 0.0, b 20, c 30 and d 60 min, UV light irradiation.

3. Result and discussion

3.1. Characterization

TEM, FT-IR, XRD, DRS and VSM techniques were utilized for the characterization of $\text{La}_2\text{MnFe}_2\text{O}_7$ and $\text{La}_2\text{CuFe}_2\text{O}_7$ nanocomposites. The phase and crystallinity of the synthesized catalysts were determined by XRD. The FT-IR spectra were recorded within the scan range of $4000\text{--}400\text{ cm}^{-1}$. The transmission electron microscopy images were used to determine the morphologies of the as-prepared nanomaterials. The magnetic properties of the synthesized catalysts were investigated using VSM. Band gap energy is determined using DRS.

The optical property of the prepared $\text{La}_2\text{MnFe}_2\text{O}_7$ and $\text{La}_2\text{CuFe}_2\text{O}_7$ nanocomposites was studied by a UV-Vis spectrophotometer. The absorbance spectra were obtained within the range of 200-600 nm.

3.1.1. FTIR analysis of $\text{La}_2\text{MnFe}_2\text{O}_7$ and $\text{La}_2\text{CuFe}_2\text{O}_7$ nanocomposites

Fig. 2 shows the FT-IR spectra of octanoic acid (a), $\text{La}_2\text{MnFe}_2\text{O}_7$ (b), as well as $\text{La}_2\text{CuFe}_2\text{O}_7$ (c) nanocomposites following calcination within the range of $400\text{--}4000\text{ cm}^{-1}$. As shown, the broad band in $2650\text{--}3450\text{ cm}^{-1}$ was associated with the O-H stretching vibration in the octanoic acid, whereas the band appeared in 1718 cm^{-1} is associated with the carbonyl group. The bending vibrations of CH_2 and CH_3 groups are observed at 1461 and 1381 cm^{-1} , respectively. The stretching band of C-O was observed at $1220\text{--}1330\text{ cm}^{-1}$ and the out of plane bending of O-H group was observed at 941 cm^{-1} . The two robust absorptive bands around 800 and 900 cm^{-1} , respectively, were associated with the M-O stretching vibration (M: metal) of $\text{La}_2\text{MnFe}_2\text{O}_7$ (b) and $\text{La}_2\text{CuFe}_2\text{O}_7$ (c). However, those around 550 and 650 cm^{-1} , respectively, were associated with the M-O bending vibration (M: metal) of $\text{La}_2\text{MnFe}_2\text{O}_7$ (b) and $\text{La}_2\text{CuFe}_2\text{O}_7$ (c). As a result, there was a similarity between the FT-IR spectra of the samples and they were consistent with those reported in the literature [27].

3.1.2. XRD analysis of $\text{La}_2\text{MnFe}_2\text{O}_7$ and $\text{La}_2\text{CuFe}_2\text{O}_7$ nanocomposites

XRD patterns of the prepared photocatalysts are exhibited in Figs. 3 and 4. The XRD analysis of $\text{La}_2\text{MnFe}_2\text{O}_7$ shows that it was possible to index the diffraction peaks to the Cubic phase ($a=8.499\text{ \AA}$, $b=8.499\text{ \AA}$, and $c=8.499\text{ \AA}$) of La_2O_3 JCPDS card 22-0641N (Fig. 3) and monoclinic phase ($a=14.60000\text{ \AA}$,

$b=3.71700\text{ \AA}$ and $c=9.27800\text{ \AA}$) of MnFe_2O_4 (JCPDS card No. 04-016-1572) with the main peak diffraction at $d=2.72\text{ \AA}$ (311 plane). XRD analysis of $\text{La}_2\text{CuFe}_2\text{O}_7$ shows that the cubic phase ($a=8.3490\text{ \AA}$, $b=8.3490\text{ \AA}$, and $c=8.3490\text{ \AA}$) is CuFe_2O_4 , JCPDS No 25-0283 (Fig. 4), and the monoclinic phase ($a=14.60000\text{ \AA}$, $b=3.7170\text{ \AA}$, and $c=9.27800\text{ \AA}$) is La_2O_3 (22-064) with a main diffraction peak at $d=2.96\text{ \AA}$ ((022) plane). The crystallite size was determined by Debye-Scherrer formula:

$$D = \frac{K\lambda}{\beta \cos\theta} \quad (1)$$

Where K ($=0.89$) signifies the shape factor, λ is the wavelength, β signifies the full width at half maximum (FWHM), and θ signifies the Bragg scattering angle [28]. The mean crystallite size was computed from the main characteristic peak of each phase, (011) located at 30.8° for La_2O_3 , (311) located at 35.5° for MnFe_2O_4 and (022) located at 30.18° for CuFe_2O_4 . The results show that for $\text{La}_2\text{MnFe}_2\text{O}_7$ nanocomposite, the crystallite size of La_2O_3 nanoparticles (8.7 nm) is significantly smaller than MnFe_2O_4 (15.77 nm). also for $\text{La}_2\text{CuFe}_2\text{O}_7$ nanocomposite, the crystallite size of La_2O_3 nanoparticles (8.7 nm) is significantly smaller than CuFe_2O_4 (13.03 nm).

It was found that the crystallite size did not change dramatically with the nature of transition metal, 8.7 , 8.7 , 15.77 and 13.03 nm for La_2O_3 in $\text{La}_2\text{MnFe}_2\text{O}_7$, La_2O_3 in $\text{La}_2\text{CuFe}_2\text{O}_7$, MnFe_2O_4 , and CuFe_2O_4 respectively.

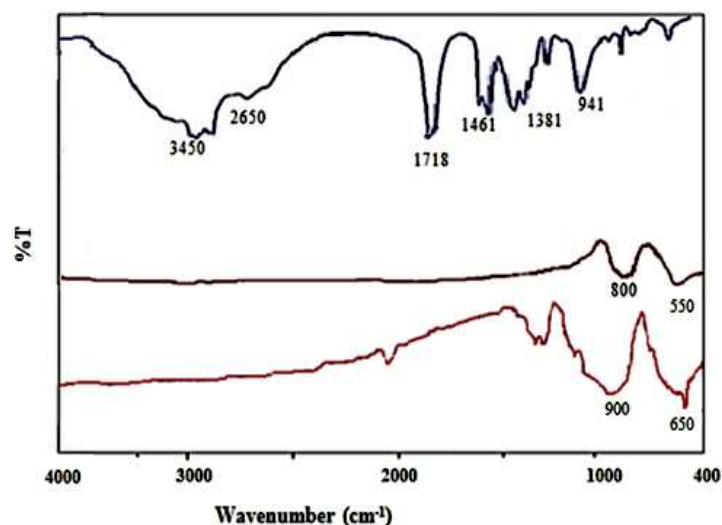


Fig. 2. FT-IR spectra of octanoic acid (a), $\text{La}_2\text{CuFe}_2\text{O}_7$ (b) and LaMnFe_2O (c) nanoparticles.

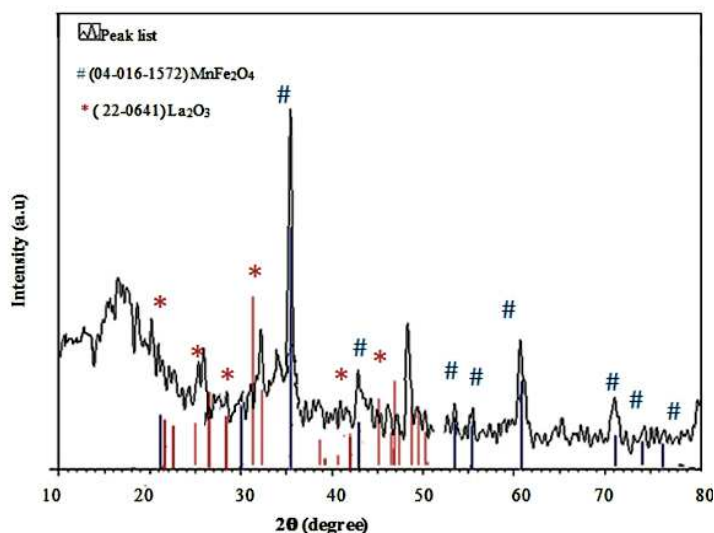


Fig. 3. XRD pattern of $\text{La}_2\text{MnFe}_2\text{O}_7$ nanoparticles.

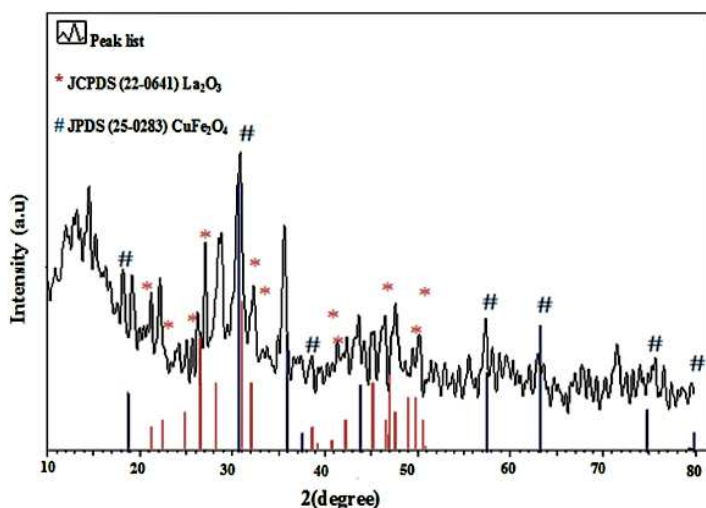


Fig. 4. XRD pattern of $\text{La}_2\text{CuFe}_2\text{O}_7$ nanoparticles.

3.1.3. TEM analysis of $\text{La}_2\text{MnFe}_2\text{O}_7$ and $\text{La}_2\text{CuFe}_2\text{O}_7$

TEM images of $\text{La}_2\text{MnFe}_2\text{O}_7$ and $\text{La}_2\text{CuFe}_2\text{O}_7$ are shown in Fig. 5. According to the TEM images, $\text{La}_2\text{MnFe}_2\text{O}_7$ and $\text{La}_2\text{CuFe}_2\text{O}_7$ catalysts are nanosized with a grain size of 20 nm, respectively. Nanoparticles possess a porous structure with a high specific area. These nanoparticles form many active positions on the surfaces. This kind of morphology with high specific area may enable more possibility to give an excellent host material for inserting and abstracting guest ions for the sake of identifying area-dependent level reactivity, and for taking action as molecular sieves [29].

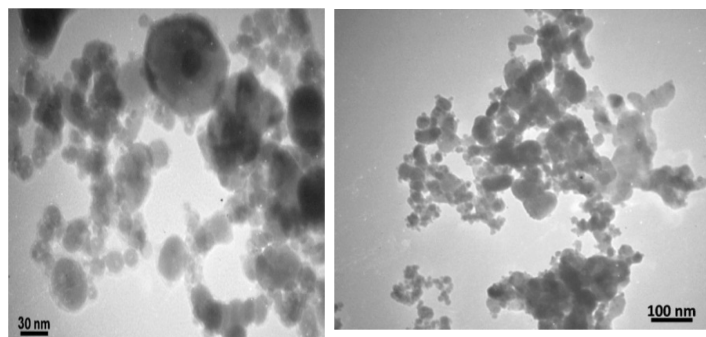


Fig. 5. TEM images of $\text{La}_2\text{CuFe}_2\text{O}_7$ (a) and $\text{La}_2\text{MnFe}_2\text{O}_7$ (b) nanocomposites.

3.1.4. DRS spectrum analysis of $\text{La}_2\text{MnFe}_2\text{O}_7$ and $\text{La}_2\text{CuFe}_2\text{O}_7$ nanocomposites

Fig. 6 shows the graph of $(\alpha h\nu)^2$ versus $h\nu$ obtained from the UV-Vis DRS spectrum of $\text{La}_2\text{MnFe}_2\text{O}_7$ and $\text{La}_2\text{CuFe}_2\text{O}_7$ nanocomposites. The corresponding band gap energy can be determined from the following equation:

$$\alpha h\nu = A(h\nu - E_g)^{\frac{1}{2}} \quad (2)$$

For direct electron transfer, A is a constant number. E_g and $h\nu$ are the energy of the direct band gap and the energy of the incident photon, respectively. The energy of the band gap is estimated to zero from the graph of $(\alpha h\nu)^2$ versus $h\nu$ by extrapolating the linear part $(\alpha h\nu)^2$. As shown in Fig. 6, the optical band gap of $\text{La}_2\text{MnFe}_2\text{O}_7$ and $\text{La}_2\text{CuFe}_2\text{O}_7$ is about 2.8 eV, which is consistent with those reported in the literature [30, 31].

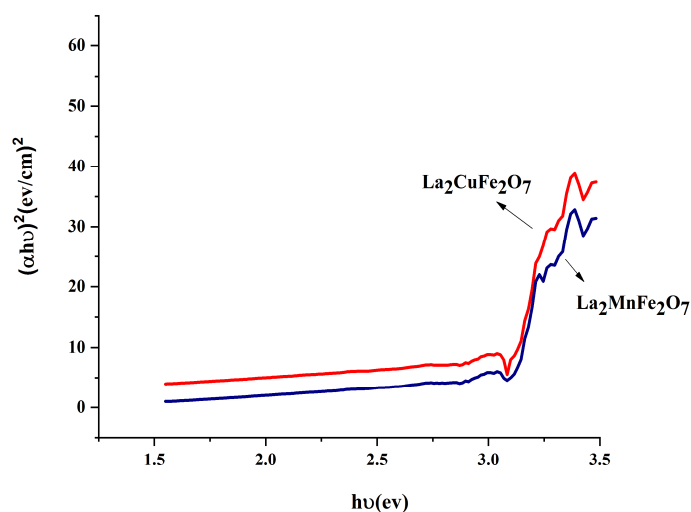


Fig. 6. The $(\alpha h\nu)^2$ versus $h\nu$ plot derived from the UV-Vis DRS spectrum of pure $\text{La}_2\text{CuFe}_2\text{O}_7$ and LaMnFe_2O composites.

3.1.5. Magnetic behavior of $\text{La}_2\text{MnFe}_2\text{O}_7$ and $\text{La}_2\text{CuFe}_2\text{O}_7$

Further elucidation on the room temperature magnetic hysteresis loops of $\text{La}_2\text{MnFe}_2\text{O}_7$ and $\text{La}_2\text{CuFe}_2\text{O}_7$ nanocomposites are presented in Fig. 7. The coercivity and saturation magnetization of $\text{La}_2\text{MnFe}_2\text{O}_7$ were measured to be 1200 Oe and 14.8 emu/g, respectively (Fig. 7a). The saturation magnetization of $\text{La}_2\text{CuFe}_2\text{O}_7$ was 0.79 emu and its coercion was almost 100 Oe (Fig. 7b) that was smaller, compared to that of $\text{La}_2\text{MnFe}_2\text{O}_7$. These two catalysts show ferromagnetic properties [32, 33].

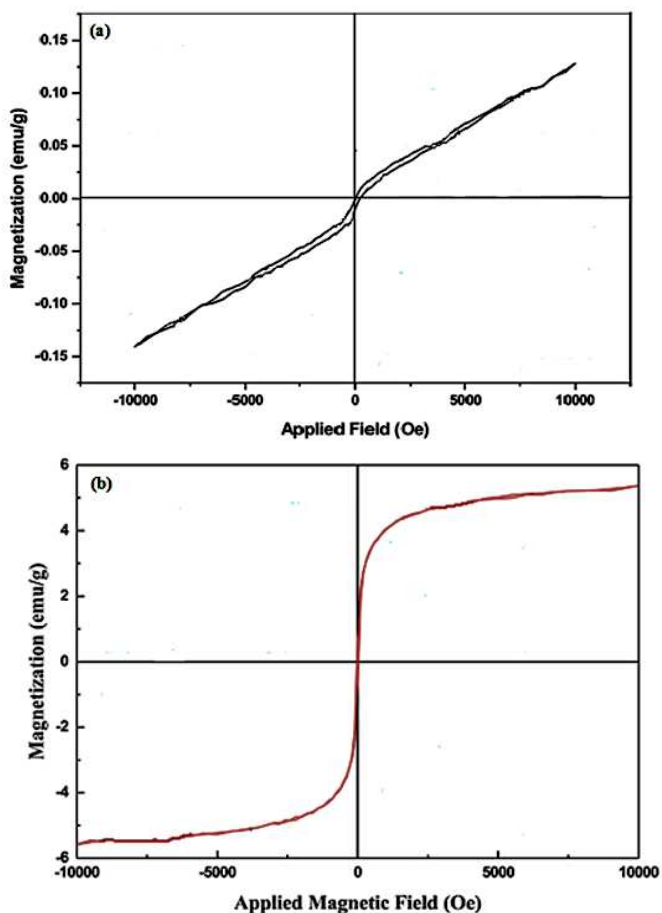


Fig. 7. Room temperature hysteresis loop of $\text{La}_2\text{MnFe}_2\text{O}_7$ (a) and $\text{La}_2\text{CuFe}_2\text{O}_7$ (b) nanocomposites.

3.2. Photodegradation of MV, MG, and EBT dyes

The degradation of MV, MG, and EBT dyes was monitored to investigate photocatalytic activity of the nanocomposites. Some factors like the solution pH, temperature, dye concentration, catalyst amount, and

irradiation time affect the optical decomposition of MG, MV, and EBT which are shown in Fig. 8a-e.

3.2.1. Effect of temperature

Fig. 8a reveals that temperature has a large effect on optical decomposition of MV, MG, and EBT. To improve the photocatalytic effect, the temperature is raised from 25 to 40 °C. With increase in temperature, the motion of dye ions increases. Thus, there was an increase in the penetration of MV, MG, and EBT ions and in the number of absorption sites after the inner structure was inflated [34].

3.2.2. Effect of MV, MG, and EBT dyes' concentrations

Fig. 8b shows the impact of the concentration of initial MV, MG, and EBT dyes upon their optical decomposition using $\text{La}_2\text{MnFe}_2\text{O}_7$ and $\text{La}_2\text{CuFe}_2\text{O}_7$ (2 mg/L) nanoparticles as absorbent. According to Fig. 8b, with an increase in the initial concentrations of MV, MG, and EBT from 1.32 to 5.28 M, the percentage of MV photodegradation using $\text{La}_2\text{MnFe}_2\text{O}_7$ and $\text{La}_2\text{CuFe}_2\text{O}_7$ reduced from 79% to 42% and 76% to 38%, respectively. For MG dye, photodegradation decreased from 72% to 36% and from 65% to 32% in the presence of $\text{La}_2\text{MnFe}_2\text{O}_7$ and $\text{La}_2\text{CuFe}_2\text{O}_7$, respectively. This photodegradation decrease for EBT dye was from 68% to 32% and from 65% to 33% using $\text{La}_2\text{MnFe}_2\text{O}_7$ and $\text{La}_2\text{CuFe}_2\text{O}_7$ nanoparticles, respectively. As the number of color molecules increased, there was a reduction in the ratio of the number of vacant sites on the surface of the catalysts to the color molecules. Thus, the entire MG, MV and EBT molecules were available at low concentrations with accessible locations on the surface of nanoparticles. With increase in the initial concentrations of dyes, active regions of the absorbent surfaces are saturated and photodegradation percent reduces [35, 36].

3.2.3. Effect of the initial pH

As shown in Fig. 8c, when the pH of solution increased, there was an increase in the photodegradation percentage of MG and MV. With increasing pH, there was a dissociation of functional groups on the adsorption surface, and there was an electrostatic attraction between the positively charged functional groups of dyes and the negatively charged groups on the surface. As a result, the optical disintegration of the dye increases [36].

3.2.4. Effect of irradiation time

The irradiation time impact on the MG and MV photodegradation using $\text{La}_2\text{MnFe}_2\text{O}_7$ and $\text{La}_2\text{CuFe}_2\text{O}_7$ (2 mg/L) as absorbents is demonstrated in Fig. 8d. The rate of photodegradation on nanocomposites was increased with an increase in irradiation time up to 60 mins. The maximum value of adsorption occurred at 60 min. Moreover, the impact of increasing time on photodegradation was not considerable because in the early stage of sorption, there were many vacant surface areas for the dye molecules, but the occupied areas started excreting the absorbing molecules in the solvent phase and in the case of absorbing molecules, to achieve the empty surface areas, the existing stimulatory forces were weakened. Thus, the sorption was decreased [37].

3.2.5. Effect of catalyst amount

As demonstrated in Fig. 8e, the photodegradation percentages of MG and MV are enhanced with an increase in the amount of $\text{La}_2\text{MnFe}_2\text{O}_7$ and $\text{La}_2\text{CuFe}_2\text{O}_7$ nanocomposites from 2.0 to 8.0 mg/L. With an increase in the catalyst value, the upper area of nanocomposites increases and $\text{La}_2\text{MnFe}_2\text{O}_7$ nanocomposites adsorb more photons on their surface, compared to $\text{La}_2\text{CuFe}_2\text{O}_7$. As a result, the absorption of dye molecules on the nanocatalyst surfaces increases and the photodegradation of MG and MV increases [38, 39].

3.2.6. Mechanism of photocatalytic degradation of MG, MV and EBT dyes

The mechanism of photocatalytic degradation of dyes under UV radiations is illustrated in Fig. 9. When UV rays excite electrons in the valence band, they transfer to the conduction band, resulting in holes in valence band, and electrons conduction band. Then they produced oxygen anion free radicals (O_2^-) and hydroxyl free radicals (OH^\cdot), respectively. Hydrogen peroxide increases the amount of free hydroxyl radicals. Therefore, this addition improves the catalytic efficiency of dye degradation [40].

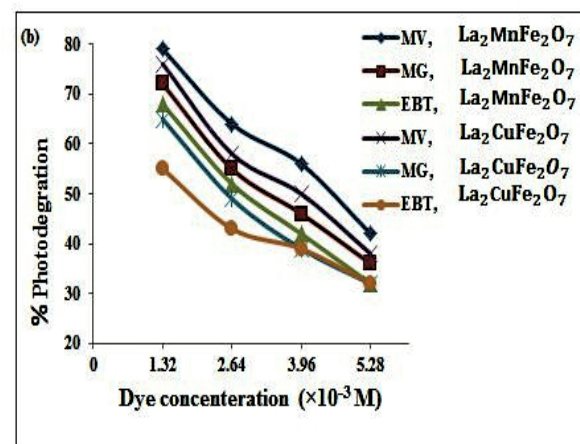
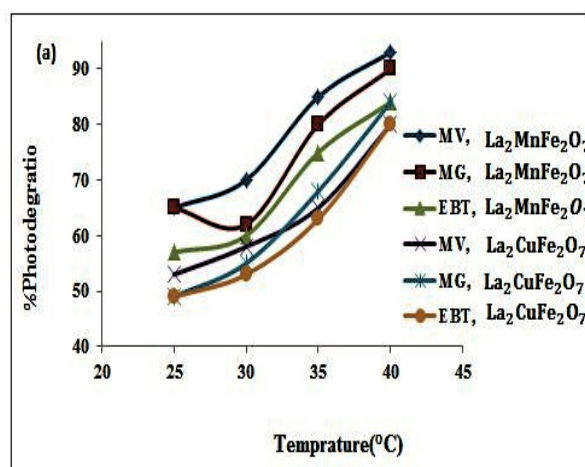
4. Conclusions

In this work, $\text{La}_2\text{MnFe}_2\text{O}_7$ and $\text{La}_2\text{CuFe}_2\text{O}_7$ nanocomposites were successfully prepared using a co-precipitation method, and characterized on the basis of FT-IR, XRD, TEM, VSM and DRS analyses. The catalytic activity of the prepared nanocomposites in the degradation of industrial dyes (MG and MV) was

investigated under the optimized conditions such as temperature (30 °C), catalyst amount (2.0 mg/L), irradiation time (60 min), dye concentration (1.59×10^{-3} M), pH (=7), and compared with each other. The present study can be a growth path for the development of photocatalytic technology, especially the recyclable magnetic photocatalysts for wastewater treatment.

Table 1 shows the performance of several synthesized photocatalysts with their experimental data [41-45]. As clarified in Table 1, the photocatalytic degradation of malachite green dye using the $\text{La}_2\text{CuFe}_2\text{O}_7$ and LaMnFe_2O composites has been compared with that of other photocatalysts reported in the literature. The results showed that $\text{La}_2\text{CuFe}_2\text{O}_7$ and LaMnFe_2O nanocomposites are superior to other catalysts for rapid and significant degradation of MG, MV and EBT dyes.

The results of photocatalytic activity of $\text{La}_2\text{MnFe}_2\text{O}_7$ and $\text{La}_2\text{CuFe}_2\text{O}_7$ nanocomposites approved the effects of both photocatalysts upon the decomposition of MV, MG and EBT dyes. However, $\text{La}_2\text{MnFe}_2\text{O}_7$ nanoparticles showed significant degradation.



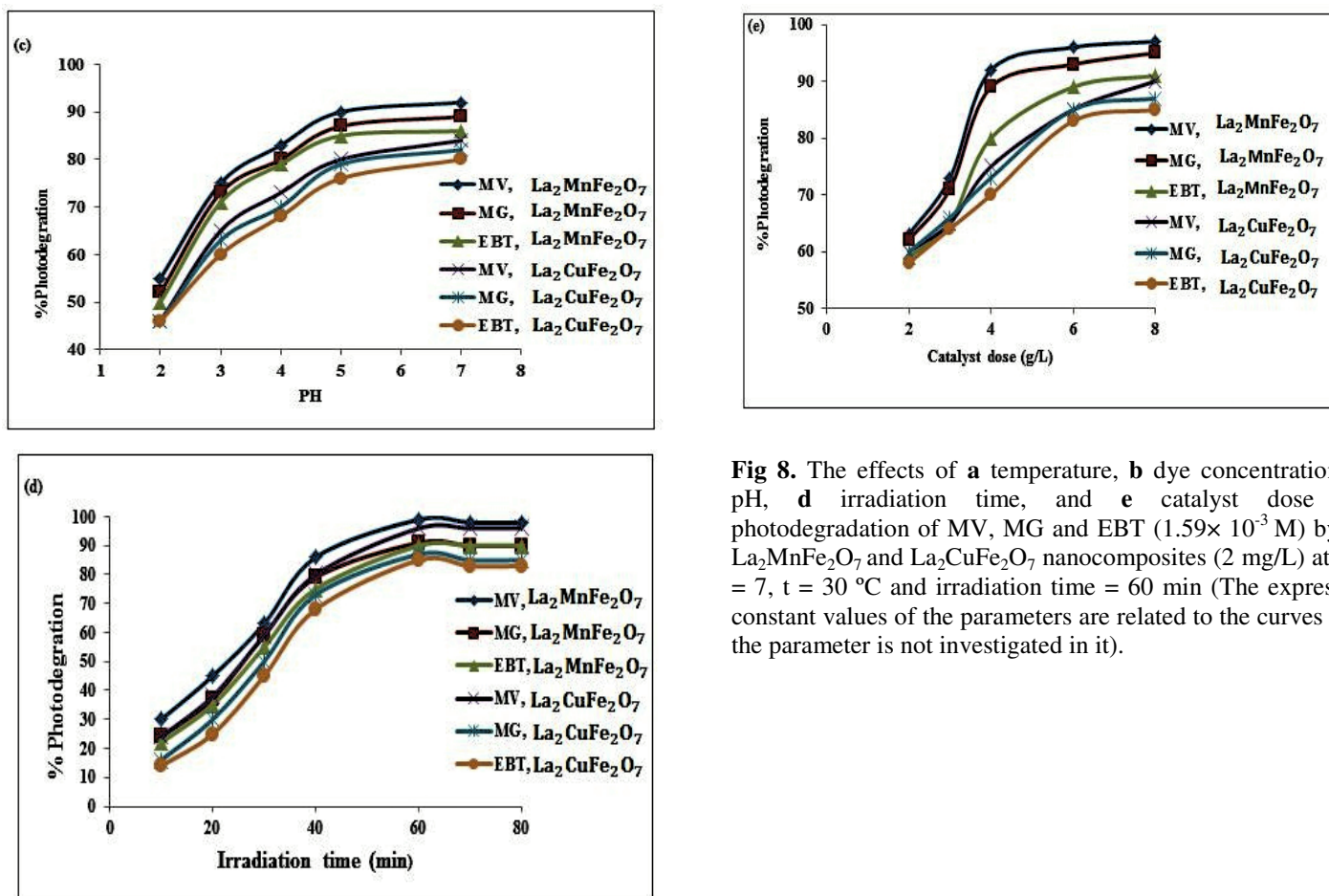


Fig 8. The effects of **a** temperature, **b** dye concentration, **c** pH, **d** irradiation time, and **e** catalyst dose on photodegradation of MV, MG and EBT (1.59×10^{-3} M) by of La₂MnFe₂O₇ and La₂CuFe₂O₇ nanocomposites (2 mg/L) at pH = 7, $t = 30$ °C and irradiation time = 60 min (The expressed constant values of the parameters are related to the curves that the parameter is not investigated in it).

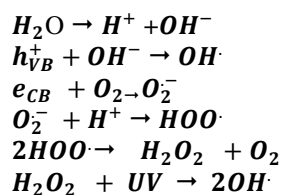
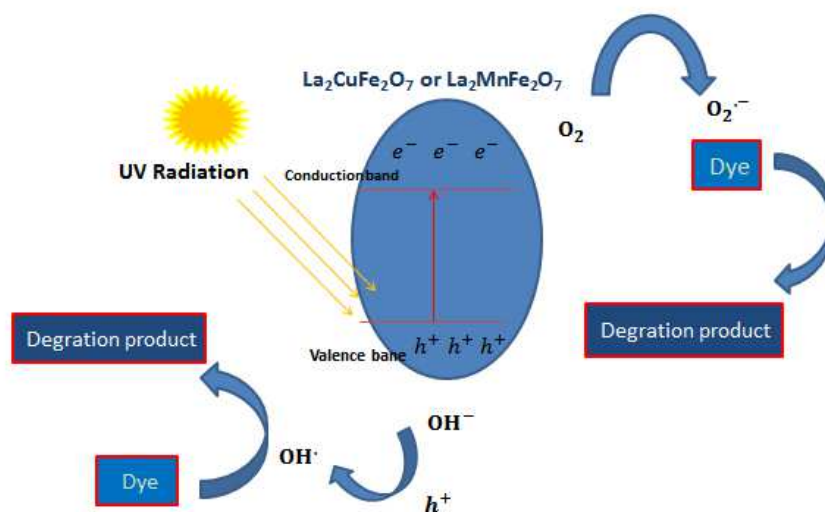


Fig. 9. A possible mechanism for the degradation of dye on the nanoparticles under UV-light irradiation.

Table 1. Degradation performance comparison of MG, MV and EBT dyes by various photocatalysts under UV irradiation.

No.	Catalysts	Target	Degradation (%)	Ref
1	Ce-B/TiO ₂	MG	90 (120 min)	[41]
2	Fe ₃ O ₄ / SiO ₂ /TiO ₂	MG	100 (150 min)	[42]
3	CeO ₂ nanoparticles	EBT	99.23 (120 min)	[43]
4	ZnO	MV	99.0 (75 min)	[44]
5	ZnS, ZnS:Fe	MV	91.4/98.8 (120 min)	[45]
6	La ₂ MnFe ₂ O ₇	MV, MG, EBT	99 MV (60 min), 91 MG (60 min), EBT 90 (60 min)	This work
7	La ₂ CuFe ₂ O ₇	MV, MG, EBT	96 MV (60 min), 87 MG (60 min), 85 EBT (60 min)	This work

Acknowledgements

We fully appreciate Payame Noor University, Islamic Azad University of Zahedan as well as Esfarayen University of Technology for providing financial and technical support.

References

- [1] (a) K.E. Yunusov, A.A. Sarymsakov, J.Z.O. Jalilov, A.A. Atakhanov, Physicochemical properties and antimicrobial activity of nanocomposite films based on carboxymethylcellulose and silver nanoparticles. *Polym. Adv. Technol.*, 32 (2021) 1822-1830; (b) G. Lavanya, T. Suvarna, C.P. Vardhani, Structural and Optical Properties of (MgZnO/rGO) Nanocomposites, *J. Chem. Lett.* 4 (2023) 136-147. 10.22034/jchemlett.2023.396420.1116; (c) A. A. Auda, H. A. J. Banimuslem, B. Y. Kadem, Photocurrent Response Characteristics of ZnO/TiO₂ Nano Thin Films on Si/SiO₂ Substrate Using Sol-Gel Method, *Chem. Rev. Lett.* 6 (2023) 513-521. 10.22034/crl.2023.425186.1260; (d) P. O. Ameh, Synthesized iron oxide nanoparticles from *Acacia nilotica* leaves for the sequestration of some heavy metal ions in aqueous solutions, *J. Chem. Lett.* 4 (2023) 38-51. 10.22034/jchemlett.2023.360137.1083.
- [2] (a) K.E. Yunusov, A.A. Sarymsakov, S.S. Rashidova, Structure and properties of biodegradable carboxymethyl cellulose films containing silver nanoparticles. *Polym. Sci. Ser. A.*, 56 (2014) 283-288; (b) P. O. Ameh, Removal of Methylene Blue from Aqueous Solution using Nano Metal Oxide Prepared from Local Nigerian Hen Egg Shell: DFT And Experimental Study, *Chem. Rev. Lett.* 6 (2023) 29-43. 10.22034/crl.2023.328721.1155; (c) M. Mosavi, Theoretical study of interaction between Mexiletine drug and pristine, Si-, Ga- and Al-doped boron nitride nano sheet, *J. Chem. Lett.* 3 (2022) 150-158. 10.22034/jchemlett.2023.384082.1103; (d) S. A. Siadati, M. Afzali, Me. Sayyadi, Could silver nano-particles control the 2019-nCoV virus?; An urgent glance to the past, *Chem. Rev. Lett.* 4 (2021) 9-11. 10.22034/crl.2020.224649.1044.
- [3] (a) M.S. Ekrami-Kakhki, A. Naeimi, F. Donyagard, Pt nanoparticles supported on a novel electrospun polyvinyl alcohol-CuO-Co₃O₄/chitosan based on *Sesbania sesban* plant as an electrocatalyst for direct methanol fuel cells. *Int. J. Hydrog. Energy.*, 44 (2019) 1671-1685; (b) D. T. Tayde, M. K. Lande, Mesoporous SiO₂-Al₂O₃: An Efficient Catalyst for Synthesis of 4,5-dihydro-1,3,5-triphenyl-1H-pyrazole, *J. Chem. Lett.* 2 (2021) 25-32. 10.22034/jchemlett.2021.274760.1022; (c) M. Edraki, I. M. Moghaddampour, E. Alinia-Ahandani, M. Banimahd Keivani, M. Sheydaei, Ginger intercalated sodium montmorillonite nano clay: assembly, characterization, and investigation antimicrobial properties, *Chem. Rev. Lett.* 4 (2021) 120-129. 10.22034/crl.2021.273340.1103; (d) S. Majedi, F. Behmagham, M. Vakili, Theoretical view on interaction between boron nitride nanostructures and some drugs, *J. Chem. Lett.* 1 (2020) 19-24. 10.22034/jchemlett.2020.106646; (e) F. P. Sejie, J. T.P Matshwele, F. M Nareetsile, V. C. Obuseng, Nanocellulose surface modification reactions and their influence on the adsorption of heavy metal ions from water -A Review, *Chem. Rev. Lett.* 6 (2023) 245-255. 10.22034/crl.2023.411755.1238.
- [4] K.E. Yunusova, A.A. Sarymsakova, F.M. Turakulova, S.S. Rashidovaa, T.L. Yurkshovichb, A.V. Kokhanb, N.K. Yurkshovichb, V.A. Alinovskayab, P.M. Bychkovskiic, N.V. Golubb, S.O. Solomevichb, Synthesis of selenium nanoparticles stabilized with sodium carboxymethylcellulose for preparation of a long-acting form of prospidine. *Russ. J. Appl. Chem.*, 94(2021) 1259-1266.
- [5] S. Khammarnia, A. Akbari, J. Saffari, M.S. Ekrami-Kakhki, Synthesis of FeLaO₃ and FeNdO₃ magnetic nanocomposites as photocatalyst for organic dye removal. *J. Clust. Sci.*, 30 (2019) 1383-1391.
- [6] K.E. Yunusova, A.A. Sarymsakova, F.M. Turakulov, Synthesis and physicochemical properties of the nanocomposites based on sodium carboxymethyl cellulose and selenium nanoparticles. *Polym. Sci. Ser. B.*, 64 (2022) 68-77.

- [7] I. Gehrke, A. Geiser, A. Somborn-Schulz, Innovations in nanotechnology for water treatment. *Nanotechnol. Sci. Appl.*, 8 (2020) 1-17.
- [8] S. Abbasi, M.S. Ekrami-Kakhki, M. Tahari, The influence of ZnO nanoparticles amount on the optimisation of photo degradation of methyl orange using decorated MWCNTs. *Prog. Ind. Ecol. Inter. J.*, 13 (2019) 3-15.
- [9] R. Roy, R.A. Roy, D.M. Roy, Alternative perspectives on “quasi-crystallinity” non-uniformity and nanocomposites. *Mater. Lett.*, 4(1986) 323-328.
- [10] D. Schmidt, D. Shah, E.P. Giannelis, New advances in polymer/layered silicate nanocomposites. *Curr. Opin. Solid State Mater. Sci.*, 6 (2002) 205-212.
- [11] H. Gleiter, Materials with ultrafine microstructures: retrospectives and perspectives. *Nanostruct. Mater.*, 1 (1992) 1-19.
- [12] M.F. Lanjwani, M.Y. Khuhawar, T.M.J. Khuhawar, A.H. Lanjwani, S.Q. Memon, W.A. Soomro, I.K. Rind, Photocatalytic degradation of eriochrome black T dye by ZnO nanoparticles using multivariate factorial, kinetics and isotherm models. *J. Clust. Sci.*, 34 (2023) 1121–1132.
- [13] R. Mohammadi, Highly Efficient catalyst of TiO₂/chitosan for Photodegradation and Sonodegradation of Organic Pollutant. *Chem Rev Lett.*, 5 (2022) 133-140
- [14] E. Forgacs, T. Cserhádi, G. Oros, Removal of synthetic dyes from wastewaters: a review. *Environ. Environ. Int.*, 30 (2004) 953-971.
- [15] E. Brillas, C.A. Martínez-Huitle, Decontamination of wastewaters containing synthetic organic dyes by electrochemical methods: An updated review. *Appl. Catal. B: Environ.*, 603-643 (2015) 166-167.
- [16] Z. Zhang, R.Y. Yang, Y.S. Gao, Y.F. Zhao, J.Y. Wang, L. Huang, J. Guo, T.T. Zhou, P. Lu, Z.H. Guo, Q. Wang, Novel Na₂Mo₄O₁₃/α-MoO₃ hybrid material as highly efficient CWAO catalyst for dye degradation at ambient conditions. *Sci. Rep.*, 4 (2014) 6797-6805.
- [17] M. Vakili, M. Rafatullah, S. Babak, A.Z. Abdullah, M.H. Ibrahim, K.B. Tan, Z. Gholami, P. Amouzgar, Application of chitosan and its derivatives as adsorbents for dye removal from water and wastewater: A review. *Carbohydr. Polym.*, 11 (2014) 115-130.
- [18] D. O. Omokpariola, Experimental Modelling Studies on the removal of crystal violet, methylene blue and malachite green dyes using Theobroma cacao (Cocoa Pod Powder). *J. Chem. Lett.*, 2 (2021) 9-24
- [19] A. Ayati, M.N. Shahrak, B. Tanhaei, M. Sillanpää, Emerging adsorptive removal of azo dye by metal-organic frameworks. *Chemosphere.*, 160 (2016) 30-44.
- [20] C.H. Xu, B.L. Zhang, Y.H. Wang, Q.Q. Shao, W.Z. Zhou, D.M. Fan, J.Z. Bandstra, Z.Q. Shi, P.G. Tratnyek, Effects of sulfidation, magnetization, and oxygenation on azo dye reduction by zerovalent iron. *Sci. Technol.*, 50 (2016) 11879.
- [21] W.H. Sun, C.J. Zhang, J. Chen, B.B. Zhang, H.Z. Zhang, Y.M. Zhang, L. J. Chen, Accelerating biodegradation of a monoazo dye acid orange 7 by using its endogenous electron donors. *J. Hazard. Mater.*, 324 (2017) 739-743.
- [22] P. Salgado, V. Melin, Y. Duran, H. Mansilla, D. Contreras, The reactivity and reaction pathway of fenton reactions driven by substituted 1,2-dihydroxybenzenes. *Environ. Sci. Technol.*, 51 (2017) 3687-3693.
- [23] F. Luo, D. Yang, Z.L. Chen, M. Megharaj, R. Naidu, One-step green synthesis of bimetallic Fe/Pd nanoparticles used to degrade Orange II. *J. Hazard. Mater.*, 303 (2016) 145-150.
- [24] K. Ancy, M.R. Bindhu, J.S. Bai, M.K. Gatasheh, A.A. Hatamleh, S. Ilavenil, Photocatalytic degradation of organic synthetic dyes and textile dyeing waste water by Al and F co-doped TiO₂ nanoparticles. *Environ. Res.*, 206 (2022) 112492.
- [25] I. Bameri, J. Saffari, S. Baniyaghoob, M.S. Ekrami-Kakhki, Synthesis of magnetic nano-NiFe₂O₄ with the assistance of ultrasound and its application for photocatalytic degradation of Titan Yellow: Kinetic and isotherm. *Colloids Interface Sci. Commun.*, 48 (2022) 100610.
- [26] F.B. Li, X. Z. Li, K.W. Cheah, Photocatalytic activity of neodymium ion doped TiO₂ for 2-mercaptobenzothiazole degradation under visible light irradiation. *Environ. Chem.*, 2(2) (2005) 130.
- [27] P.V. Gosavi, R.B. Biniwale, Pure phase LaFeO₃ perovskite with improved surface area synthesized using different routes and its characterization. *Mater. Chem. Phys.*, 119 (2010) 324.
- [28] M.K. Satheeshkumar, E. Ranjith Kumar, C. Srinivas, G. Prasad, S.S. Meena, I. Pradeep, N. Suriyanarayanan, D.L. Sastry, Sastry structural and magnetic properties of CuFe₂O₄ ferrite nanoparticles synthesized by cow urine assisted combustion method. *J. Magn. Magn. Mater.*, 484 (2019) 120125.
- [29] A. Sobhani, M. Salavati Niasari, M. Sobhani, Synthesis, characterization and optical properties of mercury sulfides and zinc sulfides using single-source precursor. *Mater. Sci. Semicond. Process.*, 16 (2) (2013) 410-417.
- [30] P. Ma, W. Jiang, F. Wang, F. Li, P. Shen, M. Chen, Y. Wang, J. Liu, P. Li, Synthesis and photocatalytic property of Fe₃O₄@ TiO₂ core/shell nanoparticles supported by reduced graphene oxide sheets. *J. Alloy Compd.*, 578 (2013) 501-506.
- [31] Q. Zhou, Z. Fang, J. Li, M. Wang, Applications of TiO₂ nanotube arrays in environmental and energy fields: A review. *Micropor. Mesopor. Mater.*, 202 (2015) 22-35.
- [32] B. Jansi Rani, B. Saravanakumar, G. Ravi, V. Ganesh, S. Ravichandran, R. Yuvakkumar, Structural, optical and magnetic properties of CuFe₂O₄ nanoparticles. *J. Mater. Sci. Mater. Electron.* 29 (2018) 1975-1984.
- [33] K. Kukli, M. Mikkor, A. Šutka, M. Kull, H. Seemen, J. Linkd, R. Stern, A. Tamm, Behavior of nanocomposite consisting of manganese ferrite particles and atomic layer deposited bismuth oxide chloride film. *J. Magn. Magn. Mater.*, 498 (2020) 166167-166172.
- [34] Y.S. Ho, T.H. Chiang, Y.M. Hsueh, Removal of basic dye from aqueous solution using tree fern as a biosorbent. *Process. Biochem.*, 40 (2005) 119-124.

- [35] C. Namasivayam, K. Thamaraiselvi, R.T. Yamuna, Removal of paraquat by adsorption on 'waste'Fe (III)/Cr (III) hydroxide: adsorption rates and equilibrium studies. *Pest. Sci.*, 41 (1994) 7-12.
- [36] Y. Subbareddy, V. Jeseentharani, C. Jayakumar, K.S. Nagaraja, B. Jeyaraj, Adsorptive removal of Malachite Green (oxalate) by low cost adsorbent. *J. Environ. Res. Develop.*, 7 (2012) 275-284.
- [37] R. Ahmad, Studies on adsorption of crystal violet dye from aqueous solution onto coniferous pinus bark powder (CPBP). *J. Hazard. Mater.*, 171 (2009) 767-773.
- [38] A. Kumar, G. Pandey, Synthesis of La:Co:TiO₂ nanocomposite and photocatalytic degradation of tartaric acid in water at various parameters. *Am. Nano Res. Appl.* 5 (2017) 40-45.
- [39] Y. Ono, T. Rachi, T. Okuda, M. Yokouchi, Y. Kamimoto, A. Nakajima, K. Okada, Kinetics study for photodegradation of methylene blue dye by titanium dioxide powder prepared by selective leaching method. *J. Phys. Chem. Solids.*, 73 (2012) 343-349.
- [40] M.A. Abdelwahab, S.M. El Rayes, M.M. Kamel, E.A. Abdelrahman, Encapsulation of NiS and ZnS in analcime nanoparticles as novel nanocomposites for the effective photocatalytic degradation of orange G and methylene blue dyes. *Int. J. Environ. Anal. Chem.*, 00 (2022) 1-18.
- [41] S. Gita, S.P. Shukla, G. Deshmukhe, T.G. Choudhury, N. Saharan, A.K. Singh, Toxicity evaluation of six textile dyes on growth, metabolism and elemental composition (C, H, N, S) of microalgae spirulina platensis: The environmental consequences. *Bull. Environ. Contam. Toxicol.*, 106 (2021) 302-309.
- [42] M. Farhadian, M. Kazemzad, Photocatalytic degradation of malachite green by magnetic photocatalyst. *Synth. React. Synth. React. Inorg. M.*, 46 (2016) 458-463.
- [43] S. Mishra, S. Soren, A.K. Debnath, D.K. Aswal, N. Das, P. Parhi, Rapid microwave-hydrothermal synthesis of CeO₂ nanoparticles for simultaneous adsorption/photodegradation of organic dyes under visible light. *Optik.*, 169 (2018) 125.
- [44] J.H. Sun, S.Y. Dong, Y.K. Wang, S.P. Sun, Preparation and photocatalytic property of a novel dumbbell-shaped ZnO microcrystal photocatalyst. *J. Hazard. Mater.*, 172 (2009) 1520-1526.
- [45] M. Shamsipur, H.R. Rajabi, Study of photocatalytic activity of ZnS quantum dots as efficient nanoparticles for removal of methyl violet: Effect of ferric ion doping. *Spectrochim. Acta A Mol. Biomol. Spectrosc.*, 122 (2014) 260-267.